ELSEVIER

Journal of Nuclear Materials 299 (2001) 43–52

journal of nuclear materials

www.elsevier.com/locate/jnucmat

Study of mechanisms involved in thermal migration of molybdenum and rhenium in apatites

C. Gaillard [a,*], N. Chevarier [a], C. Den Auwer [b], N. Millard-Pinard [a], P. Delichère [c], Ph. Sainsot [d]

[a] *Institut de Physique Nucléaire de Lyon, Université Claude Bernard, IN2P3-CNRS, 43 Boulevard du 11 Novembre 1918, F-69622 Villeurbanne cedex, France*

[b] *CEA/DRCP/SCPS/LCAM, Marcoule, BP 171, F-30207 Bagnols-sur-Cèze, France*

[c] *Institut de Recherche sur la Catalyse, av. Albert Einstein, 69622 Villeurbanne cedex, France*

[d] *Institut National des Sciences Appliquées, UMR 5514, F-69621 Villeurbanne cedex, France*

Received 21 May 2001; accepted 27 July 2001

Abstract

The aim of this work is to characterise the retention properties of apatites, studied as potential inert matrices, towards the long-lived fission product ^{99}Tc ($T = 210\,000$ years) in radioactive waste disposal. The study was made using two stable homologous elements of Tc: molybdenum which has the same mass as technetium, and rhenium which is the chemical analogue of Tc. These elements were introduced in apatite samples by ion implantation and their profiles were determined by Rutherford backscattering spectroscopy (RBS). The coupling of X-ray photoelectron spectroscopy (XPS) and X-ray absorption near-edge spectroscopy (XANES) analysis showed the oxidation of molybdenum and rhenium during annealing. Using these results on Mo and Re behaviour, assumptions were made on the migration of technetium.

PACS: 61.10.CB

1. Introduction

In the context of the high activity and long period nuclear waste management, one of the solutions considered is the storage of the waste containers in deep geological sites. The safety of the disposal will be ensured by several barriers, whose main role will be to limit the migration of radioelements in the biosphere. Among the studied materials, a close attention was paid to apatites, whose general formula is $Ca_{10}(PO_4)_6X_2$, X being a fluorine, chlorine ion or a hydroxyl group. In addition to the strong chemical and geological stability, this material has a strong ability to incorporate a wide range of elements in its crystalline structure [1,2]. It is therefore studied in order to be introduced either into waste containers as filling material or into concrete structures surrounding the containers.

The aim of this work is to obtain migration data and to understand the mechanisms involved in the thermal migration of ^{99}Tc in apatite. Indeed, ^{99}Tc, whose half-life is 2.13×10^5 years, is produced in appreciable amounts by the fission of nuclear fuel (about 1 kg of ^{99}Tc per fuel ton). In this paper, molybdenum and rhenium have been chosen as representative elements of Tc. Molybdenum was chosen because its mass (98) is very close to the ^{99}Tc one and rhenium is known to be the chemical analogue of Tc [3,4]. The behaviour of molybdenum and technetium has already been studied in spent nuclear fuel [5–7]. For molybdenum, it was shown that its migration depends on its chemical form: one part is immobilised in metallic inclusions and the other part migrates under oxidised form to the pellet–cladding interface. As for technetium, it is only present in metallic inclusions in the burn-up fuel.

* Corresponding author. Tel.: +33-4 72 43 10 63; fax: +33-4 72 44 80 04.

E-mail address: c.gaillard@ipnl.in2p3.fr (C. Gaillard).

0022-3115/01/$ - see front matter
PII: S0022-3115(01)00662-6

The first part of this paper is devoted to the migration study of molybdenum and rhenium under air annealing using Rutherford backscattering spectroscopy (RBS). In the second part, X-ray photoelectron spectroscopy (XPS) and X-ray absorption near-edge spectroscopy (XANES) measurements have been performed in order to grab structural and chemical information about molybdenum and rhenium atoms as a function of the annealing conditions.

2. Experimental method

Molybdenum and rhenium were introduced in apatite samples by ion implantation. The samples were then annealed under air at high temperature (between 300 and 550 °C) in order to enhance the migration processes. After each annealing, the profile evolution was followed by RBS which allowed us to obtain information on the Mo and Re migration mechanisms. Since molybdenum and rhenium are chemically reactive elements, we carried out XANES and XPS experiments in order to characterise their chemical state evolution during annealing.

2.1. Sample preparation

Experiments were performed on synthetic microcrystalline hydroxyapatite, referenced as DNA grade Bio-gel HTP, stacked into pellets at 0.4 GPa. The high crystallinity was confirmed by X-ray diffraction. Structural observations by scanning electron microscopy showed a high density of grain boundaries with size less than 10 nm.

Ion implantation was used to introduce ^{98}Mo and ^{187}Re in the apatite samples. It was performed at the 'Institut de Physique Nucléaire de Lyon' (IPNL). Small-angle X-ray diffraction studies have shown that ion implantation does not imply any measurable amorphisation or phase change in apatite pellets [8]. Moreover, it is known that defects created in apatite by this technique are very rapidly annealed [1,9–11]. The implanted samples were then annealed under air, between 300 and 550 °C. Table 1 resumes the implantation and annealing conditions for each sample. They were adapted to the characterisation technique used:

- For RBS experiments, we had to optimise the depth resolution in order to measure precisely ^{98}Mo and ^{187}Re evolution profiles. The implantation energy was chosen so that Mo and Re had the same range R (about 50 nm). Due to the sensitivity of the technique, we adopted a 1×10^{16} at./cm^2 fluence.
- The XPS probe is only sensitive to the first 5 nm sample surface, so it was only performed on low energy implanted samples (30 keV for Mo, 40 keV for Re corresponding to a 18 nm range).
- Due to the sensitivity of the X-ray absorption spectroscopy, we have used higher implantation fluences (5×10^{16} at./cm^2). In order to avoid sputtering, we have increased the implantation energy to 250 keV for molybdenum and 400 keV for rhenium, leading to an implanted depth in the range of 150 nm.

After implantation, the samples were annealed in air. For RBS experiments, annealings were made between 300 and 550 °C for molybdenum implanted samples and between 450 and 550 °C for rhenium implanted samples. The higher temperature was limited at 550 °C since hydroxyapatite begins to decompose beyond. In order to understand the mechanisms involved, the chemical characterisation experiments led by XPS and XANES were made with samples annealed at the lowest temperature, which corresponds to the threshold under which no profile evolution could be observed.

2.2. Characterisation techniques

2.2.1. Rutherford backscattering spectroscopy

The coupling of ion implantation and RBS was used to study molybdenum and rhenium migration in apatite.

RBS analysis was performed at IPNL, using 1.5 MeV α-particles in the case of molybdenum implanted samples and 1 MeV α-particles in the case of rhenium implanted samples. The beam current was kept equal to 3 nA in order to minimise charging and pulse pile-up effects. The surface resolution was equal to 12 nm.

2.2.2. X-ray photoelectron spectroscopy

The experiments were performed at the 'Institut de Recherche sur la Catalyse' of Lyon, using a VG Escalab

Table 1
Implantation and annealing conditions chosen in order to optimise XPS, RBS and XANES experiments

	Molybdenum analysis			Rhenium analysis		
Characterisation techniques	XPS	RBS	XANES	XPS	RBS	XANES
Implantation energy (keV)	30	100	250	40	200	400
Implantation dose (at./cm^2)	1×10^{16}	1×10^{16}	5×10^{16}	1×10^{16}	1×10^{16}	2.5×10^{16}
R (nm)	17	49	92	18	54	92
ΔR (nm)	5	15	26	4	12	21
Annealing temperature (°C)	300	300–550	300	450	450–550	450

Table 2
Mo $3d_{5/2}$ binding energies for reference compounds

Oxidation degree	Mo $3d_{5/2}$ binding energy (eV)
Mo(0)	227.8
Mo(+II)	228.4
Mo(+IV) in MoO_2	229.6
Mo(+VI) in MoO_3	232.5

Table 3
Re $4f_{7/2}$ binding energies for reference compounds

Oxidation degree	Re $4f_{7/2}$ binding energy (eV)
Re(+IV) in ReO_2	43.6
Re(+VI) in ReO_3	46.8

200R spectrometer including a hemispherical analyser adjusted at 50 eV pass energy. An Al anode (Al $K_\alpha = 1486.6$ eV) was used as the X-ray source. The presented results concern the $3d_{3/2}$ and $3d_{5/2}$ spectral lines of molybdenum and the $4f_{5/2}$ and $4f_{7/2}$ of rhenium. Charging effects were corrected using the carbon 1s line at 284.8 eV as reference energy. The energy resolution was 1 eV.

The Mo $3d_{3/2}$–Mo $3d_{5/2}$ doublet was fitted so that each peak had the same Gaussian/Lorentzian (G/L = 0.5) line shape and width. The same procedure was adopted for rhenium analysis, using the Re $4f_{5/2}$–Re $4f_{7/2}$ doublet. The deconvolution of this doublet was made considering the presence of the Ca 3s contribution, due to the apatite matrix.

After deconvolution, the species oxidation degrees were evaluated by comparison of the experimental binding energies obtained for the Mo $3d_{5/2}$ and Re $4f_{7/2}$ lines with tabulated binding energies of reference compounds [12] (cf. Tables 2 and 3).

2.2.3. X-ray absorption near-edge spectroscopy

X-ray absorption spectra of the Mo K edge and Re L_I edge were recorded at the LURE DCI storage ring (Orsay, France), operating at 1.86 GeV with an average beam current of 300 mA. A Si(3 1 1) double-crystal monochromator and an argon filled ionisation chamber detector for the incident beam were used. Energy calibration was performed with a metallic molybdenum foil, in the case of the Mo edge experiments. For rhenium analysis, energy calibration was performed at the Se K edge at 12.6 keV.

Mo $L_{II,III}$ XANES spectra were collected at station SA32 at the LURE SUPERACO storage ring (Orsay, France), using a Si(1 1 1) double-crystal monochromator. The storage ring was running at 0.8 GeV positron energy and 100–300 mA current. After each sample spectrum, energy calibration was checked by reference to metallic Mo foil and is accurate within 0.7 eV.

Two types of detection modes were used: electron total yield detection allowed us to probe the first 50 nm of the sample, while fluorescence detection gave us information on the total implanted depth (150 nm).

The intensity of the XANES spectra was normalised relatively to the atomic absorption. The residual background of each spectrum was subtracted by fitting a linear function to the pre-edge region. The energy positions of the various edge structures were determined using second derivative spectra.

3. Profile evolution under air annealing

3.1. Migration data from RBS profile evolution

The evolution of the concentration profiles of implanted species is deduced from RBS measurements as a function of annealing time. The initial profile of the as-implanted samples can be approximated by a Gaussian distribution:

$$C(x, t=0) = \frac{N_{\text{impl}}}{\sqrt{2\pi}\,\Delta R} \exp\left[-\frac{(x-R)^2}{2\,\Delta R^2}\right], \tag{1}$$

where $C(x, t=0)$ is the initial ion concentration, x is the distance from the implanted surface, N_{impl} is the implanted ion fluence, R is the mean range of the Mo or Re ions and ΔR is the range straggling.

The Gaussian distribution can evolve with time according to three independent processes, whose effects on a Gaussian distribution are schematically shown in Fig. 1:

- *Diffusion* is induced by the concentration gradient of the element. It implies a broadening of the distribution which tends to a uniform concentration over depth.
- The atomic transport in a given direction can be due to an external force, or *driving force*, which involves a shift of the atoms towards a direction x with a force

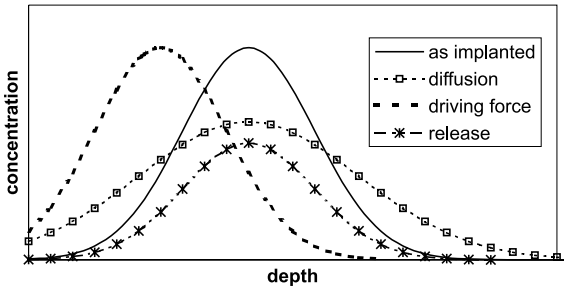

Fig. 1. Effect of diffusion, driving force towards the surface and matter release on the profile evolution of implanted species.

U. In our experiments, the driving force is due to a chemical potential gradient in the sample and leads to a shift of the whole distribution to the surface.

- The *loss of matter* is the result of an instantaneous volatilisation of the element, with a release coefficient k. It appears through a global decrease of the species concentration, without any broadening of the distribution.

These processes are independent but they can happen simultaneously. In this case, the global evolution of the species concentration C with time is given in Eq. (2):

$$\frac{\partial C}{\partial t} = D^2 \frac{\partial^2 C}{\partial x^2} + U \frac{\partial C}{\partial x} - kC, \tag{2}$$

where D is the diffusion coefficient, U is the driving force and k is the release coefficient.

In our experiments, the species evolution was due to at maximum two processes at the same time (diffusion/matter loss or driving force/matter loss).

In the case of molybdenum, the evolution of distributions with annealing time is represented in Fig. 2, at 550 °C. We can notice that the experimental range (44 nm) is slightly smaller than the value given by the TRIM code [13] (49 nm). This difference is explained by the sputtering occurring during the implantation. Nevertheless, the as-implanted profile can be approximated as a Gaussian distribution.

Molybdenum profiles evolution is characterised by a decrease in the maximum concentration. No profile shift is noted and profile broadening cannot be easily observed, implying that the diffusion is not the dominant process.

So, the molybdenum concentration evolution with annealing time is of the form

$$\frac{\partial C}{\partial t} = D^2 \frac{\partial^2 C}{\partial x^2} - kC. \tag{3}$$

For rhenium, the evolution of profiles as a function of annealing time at 550 °C is presented in Fig. 3. No profile broadening can be noted, implying that the diffusion is negligible. We can observe a slight shift towards the surface and a global decrease of the concentration.

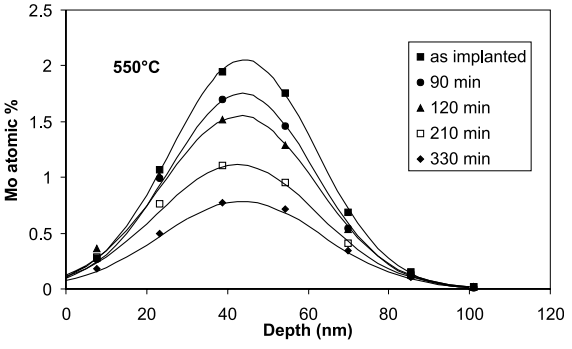

Fig. 2. Evolution of molybdenum profiles obtained by RBS after 550 °C annealing. The numerical fits are represented by lines.

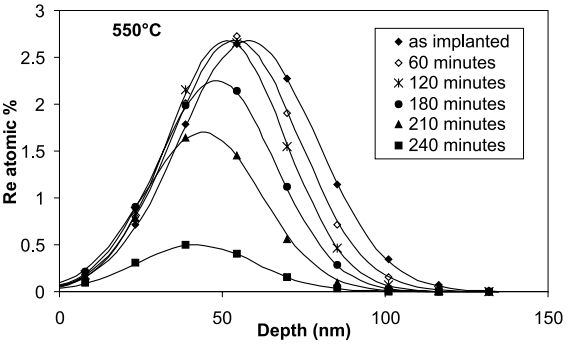

Fig. 3. Evolution of rhenium distributions obtained by RBS after 550 °C annealing. The numerical fits are represented by lines.

So, the evolution of rhenium concentration with annealing time can be written:

$$\frac{\partial C}{\partial t} = U \frac{\partial C}{\partial x} - kC. \tag{4}$$

Eqs. (3) and (4) were solved taking as initial condition the as-implanted distribution (Eq. (1)) and as boundary condition, we considered a semi-infinite medium: $C(\infty, t) = 0$.

Evermore, in the case of Eq. (3), we consider a boundary condition on the surface concentration:

$$D \frac{\partial C(0,t)}{\partial x} = K\, C(0,t),$$

where K is the surface transparency. The diffusion coefficient is very small, implying that the surface concentration is small, as it is experimentally observed.

Eqs. (2) and (3) were normalised using dimensionless variables [14], and solved by using a numerical approach, based on finite difference methods, fully described in [15].

3.2. Molybdenum evolution

We have reproduced our experimental data using Eq. (3), which takes only into account diffusion and release.

The fits are shown in Fig. 2 by lines. The so-deduced diffusion coefficients and release coefficients are presented in Table 4. No values were determined under 400 °C, the profile evolution being too weak, even for long annealing times (for instance 27 h at 300 °C). At 500 °C, $D = 5.5 \times 10^{-18}$ cm^2/s and the order of magnitude at 400 °C is 9×10^{-19} cm^2/s. Such small values indicate that the diffusion process can be neglected. Therefore we performed an analysis taking only the

Table 4
Comparison between molybdenum release coefficients: k obtained from profile evolution analysis taking into account diffusion process (D) and k_b obtained from molybdenum dose evolution, neglecting diffusion process

Annealing temperature (°C)	D (cm^2/s)	k (s^{-1})	k_b (s^{-1})
400	$(9.0 \pm 5.1) \times 10^{-19}$	$(5.3 \pm 1.4) \times 10^{-6}$	$(3.3 \pm 1.4) \times 10^{-6}$
450	$(2.5 \pm 1.7) \times 10^{-18}$	$(9.3 \pm 2.1) \times 10^{-6}$	$(7.0 \pm 2.1) \times 10^{-6}$
500	$(5.5 \pm 2.3) \times 10^{-18}$	$(1.6 \pm 0.3) \times 10^{-5}$	$(1.6 \pm 0.3) \times 10^{-5}$
550	$(1.8 \pm 0.6) \times 10^{-17}$	$(3.1 \pm 1.0) \times 10^{-5}$	$(4.1 \pm 1.0) \times 10^{-5}$

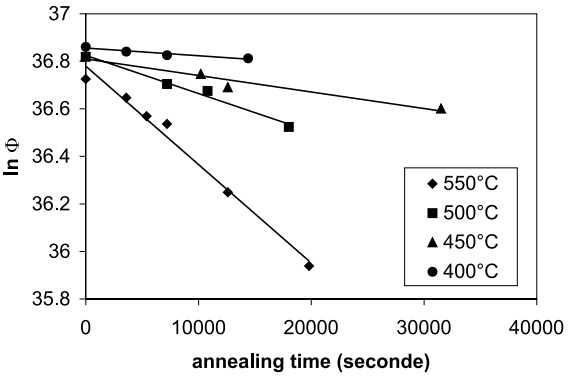

Fig. 4. Molybdenum dose evolution versus annealing time. Experimental data are represented by points. The coefficients k_b presented in Table 4 are deduced from the slope of the solid lines.

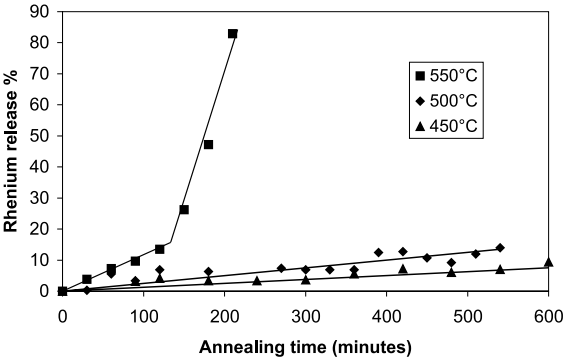

Fig. 5. Rhenium release yield as a function of annealing time. The solid lines are guide to the eye.

release process into account. The analysis was then done by considering as experimental data the molybdenum fluence Φ in the sample, obtained by the profile integration over depth, for each annealing time. The fluence evolution as a function of annealing time, for temperature between 400 and 550 °C, is presented in Fig. 4. The release coefficients, named k_b, are deduced from the slope of the straight lines. They are given in Table 4. We can notice that they are in good agreement with the values obtained from the fit of the distribution profiles.

3.3. Rhenium profile evolution

The profile fits obtained by the numerical analysis taking into account the driving force U and the release coefficient (Eq. (4)) are showed by lines in Fig. 3.

The order of magnitude of U at 550 °C is 1×10^{-3} and 6×10^{-3} nm/s at 500 °C. It cannot be determined under 500 °C annealing temperature. Thus, the driving force effect is very small, and as a consequence, cannot explain the observed rhenium release.

The rhenium release percentages versus annealing time are presented in Fig. 5. The loss varies linearly with time and it increases with temperature. For 550 °C annealing, we can observe two stages of release: the first stage, for annealing times lower than 150 min, can be correlated with the release rates measured at 450 and 500 °C. After 150 min, the change in the release kinetics is governed by a strong increase of the rhenium loss.

Table 5
Rhenium release coefficients k_b deduced from the release rate

Annealing temperature (°C)	k_b (s^{-1})
450	$(1.7 \pm 2.1) \times 10^{-6}$
500	$(3.7 \pm 0.3) \times 10^{-5}$
550	$(2.0 \pm 1.0) \times 10^{-5}$
	$(4.0 \pm 0.5) \times 10^{-4}$

The slopes of the rhenium fluence versus annealing time straight lines allowed us to deduce the release coefficients k_b for each temperature. The values are given in Table 5. They are of the same order of magnitude than those obtained for molybdenum. At 550 °C, the first value corresponds to the slow release phase and the second value to the rapid release phase.

4. Chemical characterisation

RBS analysis showed a volatilisation of molybdenum and rhenium. This loss is not a consequence of a diffusion or a driving force. These elements are not volatile at our annealing temperatures, implying that their volatilisation is due to the formation of volatile compounds. We also showed by annealing under primary vacuum

that the volatilisation depends on the amount of oxygen in the annealing atmosphere. Therefore, in order to understand the mechanisms responsible for the volatilisation, we carried out the chemical analysis of molybdenum and rhenium. These studies were made at low temperature, so that we would follow the formation of the volatile species before their volatilisation.

XPS analysis allowed us to obtain the evolution of oxidation degree of rhenium and molybdenum at the very near surface (5 nm). Moreover, XANES studies gave us information on the structure of the compounds formed during annealing, the detection modes were chosen in order to probe either the whole implanted depth (150 nm) or only part of the implanted depth (50 nm).

4.1. X-ray photoelectron spectroscopy

The oxidation states of the Mo and Re implanted samples were determined using the Mo $3d_{3/2}$–Mo $3d_{5/2}$ and Re $4f_{5/2}$–$4f_{7/2}$ doublets. Since this technique probes only the first 5 nm of the sample, we used low energy implanted hydroxyapatite pellets.

4.1.1. Molybdenum

The results are presented in Fig. 6 for an as-implanted sample and a 300 °C annealed sample. On the as-implanted sample (Fig. 6(a)), two oxidation states at 229.7 and 231.1 eV binding energies can be observed. Comparing with reference compound energies (Table 2) [16], they can be assigned, respectively, to Mo(+IV) and to an intermediate oxidation state, noted x where $+\mathrm{IV} < x < +\mathrm{VI}$. After annealing, molybdenum is also present under two oxidation states. The main one at 232.4 eV with a 81% ratio corresponds to Mo(+VI). The 19% left can be assigned to an oxidation state standing between (+IV) and (+VI). We can conclude that molybdenum oxidises during air annealing to Mo(+VI).

4.1.2. Rhenium

Fig. 7 presents the spectra obtained for the as-implanted sample (Fig. 7(a)) and a 450 °C annealed sample (Fig. 7(b)). The binding energies of the $4f_{7/2}$ contribution are, respectively, 42.6 eV for the as-implanted sample and 46.0 eV for the annealed sample. Comparing with reference data (Table 3), we can assume that after implantation, the rhenium oxidation degree is close to (+IV). During air annealing, rhenium is oxidised to Re(+VI).

So, XPS analysis showed an oxidation of molybdenum and rhenium to the oxidation degree (+VI) during air annealing. But, this technique probes only the extreme surface of the sample and gives no structural information on the Mo and Re environment. We use XANES analysis in order to get more information.

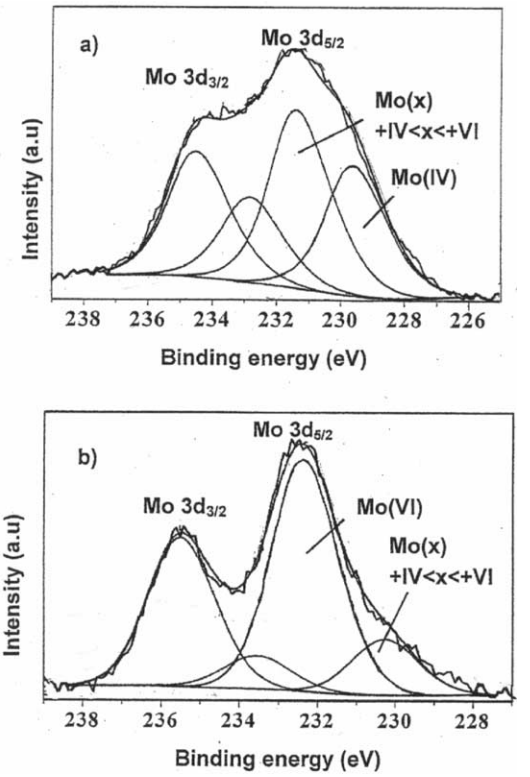

Fig. 6. Mo(3d) spectra with signal shape analysis: (a) as-implanted sample and (b) after 4 h 30 min annealing at 300 °C.

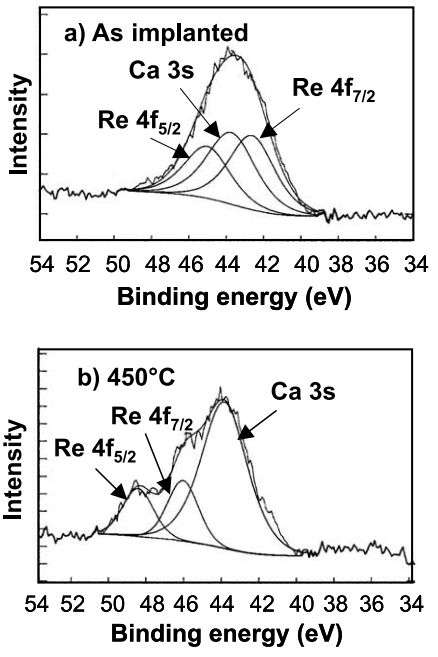

Fig. 7. Re(4f) spectra with signal shape analysis: (a) as-implanted sample and (b) after 450 °C annealing.

4.2. X-ray absorption near-edge spectroscopy

We have carried out XANES analysis for many reasons: it probes a larger depth than XPS, and gives not only oxidation degree but also structural information on the element.

The edge shapes and energies of the Mo K, L_{II} and L_{III} edges were compared with the reference compound spectra. The latter were chosen in order to evaluate the influence of oxidation degree and coordination on the XANES spectra. Thus, the reference compounds chosen for the Mo XANES characterisation were MoO_2, MoO_3 and Na_2MoO_4. MoO_2 is composed of octahedral MoO_6 units, molybdenum having a (+IV) oxidation degree. In MoO_3, composed of distorted octahedrals units, Mo has a (+VI) oxidation degree. For Na_2MoO_4, in which Mo is also (+VI), it is composed of tetrahedral (MoO_4) units [17–19].

The same approach was adopted for the Re L_I-edge experiments. The reference compounds chosen were ReO_2, composed of octahedral ReO_6 units in which Re has a (+IV) oxidation degree; ReO_3 in which the octahedra are slightly distorted to a tetrahedral structure and Re has a (+VI) oxidation degree, and $KReO_4$, formed by tetrahedral units in which Re has a (+VII) oxidation degree [20–23].

4.2.1. Molybdenum

4.2.1.1. Analysis of XANES spectrum of implanted hydroxyapatite at the molybdenum K edge. We have chosen fluorescence detection, in order to have information representative of the total implanted depth (150 nm).

The spectrum obtained on a 300 °C annealed sample for 5 h is represented in Fig. 8 and compared with the reference spectra. The pre-peak observed on the Na_2MoO_4 compound can be attributed to the $1s \rightarrow 4d$ transition, permitted for tetrahedral compounds [24,25]. For MoO_3, composed with distorted octahedrals, we can observe a slight shoulder. In our sample, neither pre-peak nor shoulder is observed at the pre-edge region, meaning that molybdenum is not in tetrahedral or distorted octahedral sites. Comparing the edge position for our sample (20 024 eV) with the references (Table 6), it is close to the one of MoO_2 edge energy (20 026 eV). Therefore, molybdenum is present in our sample as Mo(+IV), most likely in the MoO_2 form.

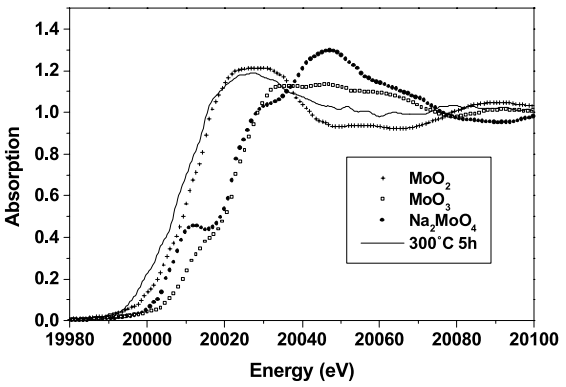

Fig. 8. Comparison at the Mo K edge spectra of reference compounds (MoO_2, MoO_3 and Na_2 MoO_4) and of an Mo implanted hydroxyapatite sample annealed at 300 °C.

Table 6
Mo K edge energy position for molybdenum reference compounds

Reference compounds	Edge energy (eV)
MoO_2	20 026
MoO_3	20 034
Na_2MoO_4	20 030

4.2.1.2. Analysis of XANES spectrum of implanted hydroxyapatite at the molybdenum $L_{II,III}$ edges. The predominant feature of the Mo L-edge XANES spectrum is an intense white line corresponding to the $2p_{3/2,5/2} \rightarrow 4d_{3/2,5/2}$ transition. These transitions probe the 4d valence orbitals participating in the Mo–O bond and are thus very sensitive to the Mo environment. Spectra could not be recorded in fluorescence mode because of a too high signal to noise ratio and we had to use the total yield mode, which probes the first 50 nm of the sample.

Fig. 9 presents the spectrum obtained on a 300 °C annealed sample for 5 h. It is compared with the reference compound spectra. For the latter, the presence of the A–B doublet is attributed to the 4d splitting under oxygen atom field into t_{2g} and e_g^* molecular orbitals for octahedral compounds and e and t_2^* molecular orbitals for tetrahedral compounds [24,26]. The relative intensity of A and B is a function of the transition probability ($t_{2g}/e_g^* = 3/2$ and $e/t_2^* = 2/3$). In our samples, the presence of the A–B doublet is observed, but there is an inversion of the relative intensity of the two contributions for the L_{II} and the L_{III} edges. Since these spectra do not correspond to any reference spectra, we fitted them with a linear combination of the reference spectra. Best fit was obtained using a weight of MoO_3 (O_h) and Na_2MoO_4 (T_d) reference spectra and is presented in Fig. 10. Therefore, molybdenum is present in the first 50 nm of the sample as Mo(+VI) with 40% in octahedral site and 60% in tetrahedral site.

4.2.2. Rhenium

XANES analysis was carried out at the L_I edge, corresponding to the $2s^26p^n \rightarrow 2s^16p^{n+1}$ dipolar transition. Indeed, the K edge of rhenium (71 662 eV) is not

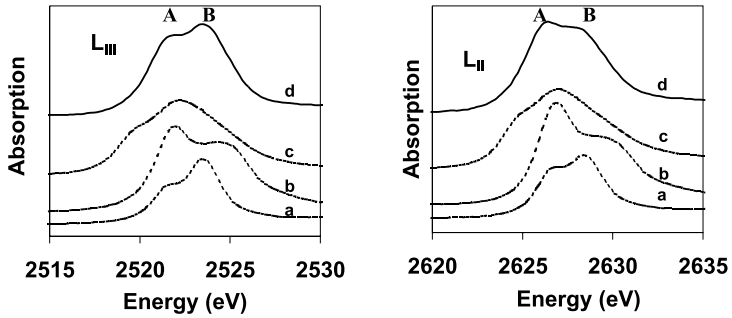

Fig. 9. XANES Mo $L_{II,III}$ edge spectrum of (a) Na_2MoO_4, (b) MoO_3, (c) MoO_2 and (d) Mo implanted hydroxyapatite sample annealed at 300 °C for 5 h.

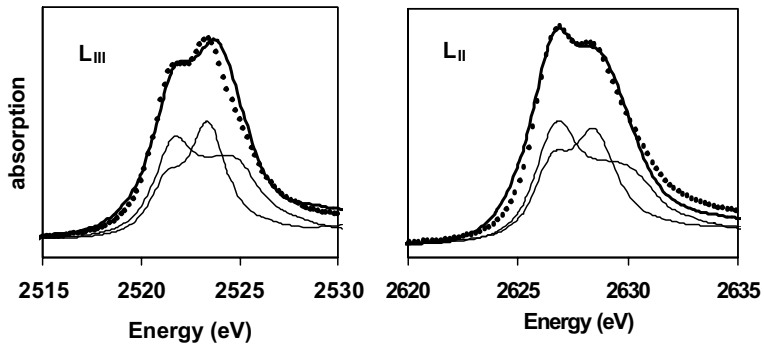

Fig. 10. XANES experimental spectrum (bold line) of 300 °C annealed sample modelled (dotted) by a mixture of 40% octahedral and 60% tetrahedral form (line).

accessible experimentally. However, the L_I edge feature is comparable to the Mo K edge feature, given the increase of the core hole. For instance for the tetrahedral compound $KReO_4$ model compound (Fig. 11), a pre-edge peak due to the $2s \rightarrow 5d$ transition is observed accounting for the tetrahedral environment of Re. This pre-edge peak is absent in the edge spectrum of ReO_2 in which Re is in an octahedral symmetry and we can notice a slight shoulder for ReO_3, formed by slightly distorted octahedrals [27]. We have also represented in Fig. 11 the XANES spectrum obtained for a 450 °C annealed sample. Neither pre-peak nor shoulder can be observed, meaning that rhenium is in a octahedral site. Moreover, comparing the edge energy position with the reference compound ones (Table 7), we can conclude that rhenium is present in our sample as Re(+IV) in a form close to ReO_2.

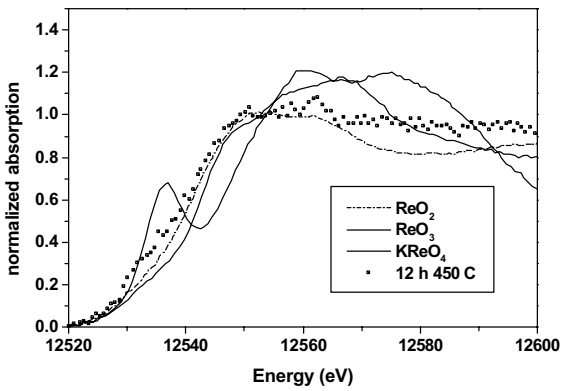

Fig. 11. Re L_I edge XANES spectra: comparison between reference compounds and a 450 °C annealed hydroxyapatite sample implanted in rhenium.

5. Discussion

The evolution of molybdenum and rhenium implanted in hydroxyapatite is characterised by a volatilisation of these elements during air annealing. We showed by XPS and XANES analysis that this volatilisation was tied to an oxidation of molybdenum and rhenium during annealing.

The results obtained by XPS and XANES are summarised in Fig. 12. We took advantage of the complementary depth analysis given, respectively, by XPS (very

Table 7
Rhenium L_I edge energy for reference compounds

Reference compounds	Edge energy (eV)
ReO_2	12 554
ReO_3	12 567

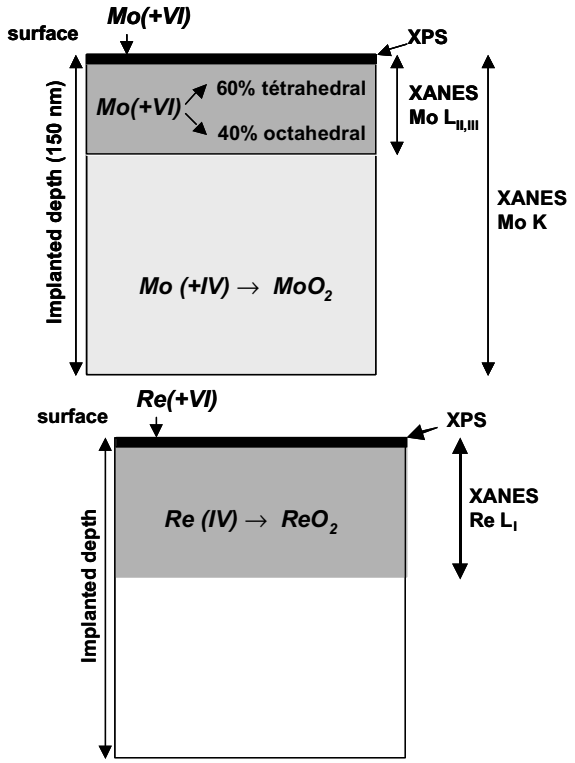

Fig. 12. Chemical evolution of molybdenum and rhenium during annealing – results of XPS and XANES analyses.

near surface analysis method), the L edge XANES electron detection probing the first 50 nm of the implanted depth and the K edge XANES fluorescence taking into account the whole implantation depth (150 nm). The combination of all these results showed first an Mo and Re oxidation gradient as a function of depth. We can conclude from these results that the oxidation is achieved by a sequential reaction mechanism:

- In the case of molybdenum, the first oxide formed is MoO_2, in which molybdenum has a (+IV) oxidation degree and an octahedral coordination. With time, this oxide transforms to a Mo(+VI) compound in which molybdenum has two types of symmetry, octahedral and tetrahedral. It is known that molybdenum oxides are composed either of tetrahedron MoO_4^{2-} (molybdate) or/and octahedron [MoO_6]. In MoO_3, molybdenum is in an octahedral site, but the octahedra are so distorted that some authors consider that this oxide is formed by tetrahedron chains [28]. This phenomenon can explain the XANES $L_{II,III}$ results, and we can assume that the final oxide formed is probably MoO_3.
- The first rhenium oxide showed by XANES is ReO_2. Considering that it evolves to an Re(+VI) compound, we can assume that it oxidises with time to ReO_3. This oxide is not volatile at our annealing temperatures. The most volatile rhenium oxide is Re_2O_7, where rhenium has a (+VII) oxidation degree. The fact that this compound is very volatile (above 250 °C) may explain that we have not found any Re(+VII) species in our sample, Re_2O_7 probably volatilises as soon as it is formed.

The molybdenum and rhenium oxidation is the consequence of the presence of oxygen in the annealing atmosphere. So, it is correlated to the oxygen diffusion in our sample. The oxygen diffusion in apatite was studied in fluoroapatite single crystals [29]. The results indicate that, at 500 °C, the diffusion velocity in single crystal apatite is 6 nm/min. In our polycrystalline apatite, the diffusion is enhanced by the high grain boundaries density. So the oxygen velocity in our sample is not a limiting factor to oxidation. Nevertheless, the fact that oxygen diffusion is a rapid process does not mean that the amount of oxygen diffusing in our sample is large enough to allow a complete oxidation of molybdenum and rhenium. This phenomenon could explain the oxidation gradient observed for Mo and Re.

The evolution of Mo and Re profiles with annealing time, characterised by RBS, allowed us to measure the release coefficient of these elements for each annealing temperature. The Arrhenius plot, deduced from these results, is represented on Fig. 13. Release activation energies are 0.7 eV/at. for Mo and 1.2 eV/at. for Re. These values, indicating that the Mo release is energetically easier than the Re release, confirm the experimental observations on the release rate of the elements. The matter loss is due to the oxidation followed by a

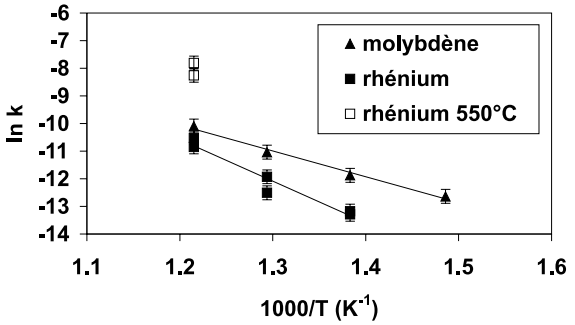

Fig. 13. Release Arrhenius plot for molybdenum and rhenium implanted in hydroxyapatite. In the case of rhenium, the empty square points represent the fast release phase at 550 °C.

volatilisation. This last process is instantaneous, meaning that the activation energy of volatilisation is very small. So, the release activation energies correspond mainly to oxidation activation energies. As far as the annealing temperature is high enough to allow a volatilisation of the oxidised species, the release process is led by the oxidation, the slowest process.

These experiments were made in order to get information on the technetium migration behaviour in apatite. They showed that Mo and Re behaviour is led by the formation of oxidised volatile species, so, by their chemical affinity with oxygen. Since rhenium is the chemical analogue of technetium, we can assume that the Tc behaviour will be also led by its oxidation in Tc_2O_7, volatile at ambient temperature. Moreover, we showed the importance of the migration of oxygen in the matrix. In order to show the dependence of grain boundaries on the oxidation and volatilisation processes, studies on sintered hydroxyapatite pellets will be led.

Acknowledgements

The authors would like to thank A. Plantier for the implantations and the IPNL accelerator team. They also thank A.M. Flanck for his participation in the XANES experiments.

References

[1] J. Carpena, J.-L. Lacout, L'Actualité Chimique 2 (1997) 3.
[2] P. Martin, G. Carlot, A. Chevarier, C. Den Auwer, G. Panczer, J. Nucl. Mater. 275 (1999) 268.
[3] J.G. Darab, P.A. Smith, Chem. Mater. 8 (1996) 1004.
[4] K. Schochau, Radiochim. Acta 32 (1983) 139.
[5] I. Sato, H. Furuya, K. Idemitsu, T. Arima, K. Yamamoto, M. Kajitani, J. Nucl. Mater. 247 (1997) 46.
[6] H. Bailly, D. Ménessier, C. Prunier, Le combustible nucléaire des réacteurs à eau sous pression et des réacteurs à neutrons rapides, Collection CEA, 1996.
[7] H. Kleykamp, J. Nucl. Mater. 131 (1985) 221.
[8] P. Martin, A. Chevarier, G. Panczer, J. Nucl. Mater. 278 (2000) 202.
[9] W. Ritter, T.D. Märk, Nucl. Instrum. and Meth. B 14 (1986) 314.
[10] F. Villa, Thesis, Université de Franche Comté, 1997.
[11] I.R. Duddy, P.F. Green, G.M. Laslett, Chem. Geol. (Isotope Geoscience Section) 73 (1988) 25.
[12] J.F. Moulder, W.F. Stickle, P.E. Sobol, K.D. Bomben, in: J. Chaspain (Ed.), Handbook of X-ray Photoelectrons Spectroscopy, Perkin Elmer, Eden Prairie, 1992.
[13] J.F. Ziegler, J.P. Biersack, U. Littmark, The Stopping and Range of Ions in Solids, Pergamon, Oxford, 1985.
[14] C. Gaillard, N. Chevarier, N. Millard-Pinard, P. Delichère, Ph. Sainsot, Nucl. Instrum. and Meth. B 161–163 (2000) 646.
[15] J. Crank, The Mathematics of Diffusion, 2nd Ed., Claredon, Oxford, 1975.
[16] I. Peeters, A.W. Denier van der Gon, M.A. Reijme, P.J. Kooyman, A.M. de Jong, J. Van Grondelle, H.H. Brongersma, R.A. van Santen, J. Catal. 173 (1998) 28.
[17] T. Ressler, O. Timpe, T. Neisius, J. Find, G. Mestl, M. Dieterle, R. Schlögl, J. Catal. 191 (2000) 75.
[18] B. Resiak, Thesis, Université de Bourgogne, 1990.
[19] L.M. Von Hippel, F. Hilbrig, H. Schmelz, B. Lengeler, H. Knözinger, Collect. Czech. Chem. Commun. 57 (1992) 2465.
[20] M. Fröba, thesis, Université d'Hambourg, 1993.
[21] A. Kuzmin, J. Purans, G. Dalba, P. Fornasini, F. Rocca, J. Phys. Condens. Matter. 8 (1996) 9083.
[22] G. Dalba, P. Fornasini, A. Kuzmin, J. Purans, F. Rocca, J. Phys. Condens. Matter. 7 (1995) 1199.
[23] A. Kuzmin, J. Purans, M. Benfatto, C.R. Natoli, Phys. Rev. B 47 (5) (1993) 2480.
[24] H. Aritani, T. Tanaka, T. Funabiki, S. Yoshida, K. Eda, N. Sotani, M. Kudo, S. Hasegawa, J. Phys. Chem. 100 (1996) 19495.
[25] R.G. Leliveld, A.J. Van Dillen, J.W. Geus, D.C. Koningsberger, J. Catal. 165 (1997) 184.
[26] S.R. Bare, G.E. Mitchell, J.J. Maj, G.E. Vrieland, J.L. Gland, J. Phys. Chem. 97 (1993) 6048.
[27] M. Fröba, K. Lochte, W. Metz, J. Phys. Chem. Solids 57 (5) (1996) 635.
[28] G. Mestl, T.K.K. Srinivasan, H. Knözinger, Langmuir 11 (1995) 3795.
[29] B.S.H. Royce, J. Phys. (Paris) 34 Colloq. C9 (1973) 327.